Sensors and Materials, Vol. 38, No. 1 (2026) 13–26
MYU Tokyo

S & M 4281

Design and Performance Analysis of Hydrophilic Rubber Soil Moisture Sensor Based on Fiber Bragg Grating

Zhitao Gao,[1,2] Bailin Rao,[1] Fenfen Yan,[1*] and Jianxian Cai[1,2,3]

[1]Institute of Disaster Prevention, Sanhe, Hebei 065201, China
[2]Hebei Key Laboratory of Seismic Disaster Instrument and Monitoring Technology, Sanhe, Hebei 065201, China
[3]Langfang Key Laboratory of Accurately-Controlled Active Seismic Source, Sanhe, Hebei 065201, China

(Received September 1, 2025; accepted December 4, 2025)

Keywords: soil moisture, fiber Bragg grating, hydrophilic rubber, performance analysis

To address the need for the long-term and stable monitoring of regional soil moisture in challenging outdoor power supply situations, a soil moisture sensor based on an expansion-type fiber Bragg grating (FBG) was developed. The sensor's sensing element was fabricated from a hydrophilic rubber material. Three different rubber probe head structures were tested and compared to ensure that the mesh-penetrating rubber probe head was selected for its superior water absorption and desorption characteristics, monotonicity, and sensitivity. The effects of temperature on the sensor's measurement results were analyzed, and temperature compensation was implemented using a dedicated FBG with a thermal sensitivity of 0.35 pm/K. The dynamic response performance of the sensor was evaluated using a spectrometer, which showed response times of 5 h for the water absorption phase and 8 h for the desorption phase. The sensor's effective output wavelength ranged from 1557.711 to 1557.642 nm. To validate its effectiveness, Beijing's sandy loam soil was used as a test sample, and linear regression analysis was conducted between sensor output values and corresponding measurements. This analysis yielded a coefficient of determination (R^2) of 0.9659, indicating a strong linear relationship. Utilizing this designed sensor, we established a soil moisture measurement system that enables long-term and stable monitoring in regional contexts even under challenging outdoor environments. Field tests confirmed that this sensor enables reliable, long-term monitoring with high immunity to external interference and independence from local power supplies.

1. Introduction

Soil moisture monitoring is a critical component of precision irrigation in automated agriculture.[1–3] Established methods for soil moisture measurement include the drying method, tensiometry, and resistance- and dielectric-based techniques.[4] Although widely applied, these conventional methods exhibit inherent limitations. Specifically, they face challenges in achieving long-term, stable, regional monitoring, particularly in power-limited field environments. For instance, the drying method is only suitable for laboratory measurements;

*Corresponding author: e-mail: 337856275@qq.com
https://doi.org/10.18494/SAM5893

ISSN 0914-4935

tensiometry and resistance-based methods are susceptible to variations in soil salinity and physicochemical properties, which compromises their long-term stability and ability to achieve long-term stable detection; and the regional deployment of dielectric sensors necessitates extensive cabling and a consistent power supply.[5–7]

With advancements in sensing technology, fiber Bragg grating (FBG) sensors have been widely adopted in various fields owing to their intrinsic advantages, including small size, corrosion resistance, high sensitivity, strong anti-interference capability, long transmission distance, and capacity for quasi-distributed networking.[8–11] The broad applications of photonic sensors, including FBG technology, in environmental and agricultural monitoring have been extensively reviewed, highlighting their growing importance in these fields.[12] Currently, FBG-based soil moisture sensors are predominantly categorized into two types: active-heating and coating-based sensors. Active-heating FBG sensors generally measure soil moisture through changes in temperature characteristics. Because of the distributed networking characteristics of FBGs, this method enables regional soil moisture measurement, but this approach requires significant power for heating, limiting its application in power-constrained field settings.[13–15] Conversely, coating-based sensors that employ moisture-sensitive coatings (e.g., polyimide, polyvinyl alcohol) to induce strain upon water absorption do not require an external power supply. However, the direct coupling between a water-sensitive coating and an FBG results in poor repeatability and long-term stability owing to the nonuniform expansion and degradation of the coating material.[14,16–18] Recent reviews have confirmed these challenges and the limited application of FBGs in agriculture.[19] Therefore, there is a significant need to design a soil moisture sensor that is stable, robust to interference, and suitable for long-term, regional monitoring under challenging field conditions.This research gap is further confirmed by recent comprehensive reviews, highlighting that a consolidated focus on robust sensors for soil water content in agriculture remains a key research gap.[20]

To address these limitations, in this paper, we present the design and characterization of a novel expansion-based soil moisture sensor. The proposed device integrates an FBG with a hydrophilic polymer rubber,[21] leveraging the material's hygroscopic expansion to induce a measurable strain on the FBG.

2. Structural Design and Measurement Principle of the Sensor

2.1 Structural design

As shown in Fig. 1, the proposed expansion-based FBG soil moisture sensor is primarily composed of a fiber optic cable, a temperature-compensating grating, a tension spring, an aluminum alloy casing, a strain-sensing grating, permeable holes, a hydrophilic rubber probe, and a polyurethane mesh.

A single optical fiber features two inscribed grating regions: a strain-sensing grating and a temperature-compensating grating. A UV-curable adhesive is employed for all bonding procedures. The optical fiber is bonded to the hydrophilic rubber probe and the tension spring at points c and d, respectively. The tension spring applies a preliminary tensile stress to the strain-

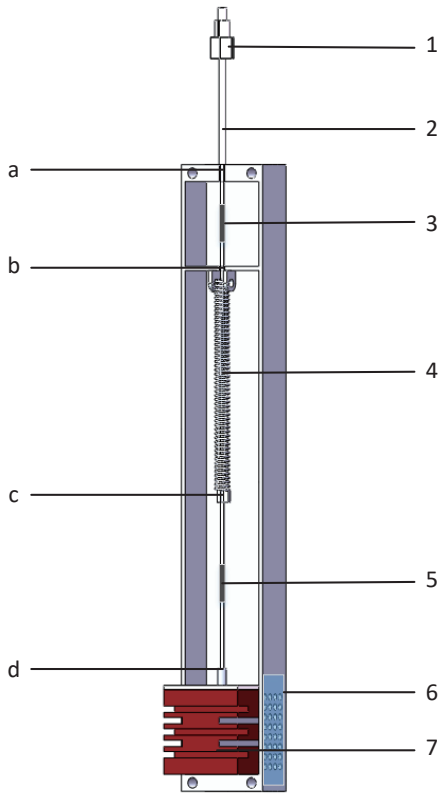

Fig. 1. (Color online) Sensor structure design. 1. Ferrule Connector (FC) interface; 2. Armored fiber optic cable; 3. Temperature grating; 4. Spring; 5. Strain grating; 6. Polyurethane mesh; 7. Hydrophilic rubber probe.

sensing grating. To isolate the temperature-compensating grating from mechanical strain, the optical fiber is anchored to the aluminum alloy casing at bonding points a and b. Soil moisture infiltrates the sensor's interior through a permeable hole (0.1 cm in diameter) at the bottom of the casing, causing the hydrophilic rubber probe to swell. A polyurethane mesh is placed over the exterior of this hole to prevent particulate impurities from compromising measurement accuracy.

2.2 Principles of measurement

Different soil volumetric water contents result in different axial expansions of the hydrophilic rubber probe. The spring elongation is equal to the axial expansion of the hydrophilic rubber probe. According to the sensing principle of the FBG, the expression for its central wavelength is[22]

$$\frac{\Delta\lambda_\beta}{\lambda_\beta} = \left(a + \zeta\right)\Delta T + \left(1 - p_e\right)\Delta\varepsilon, \tag{1}$$

where a is the coefficient of expansion, ζ is the thermal-optic coefficient, p_e is the elasto-optic coefficient, $\Delta\varepsilon$ is the axial strain of the FBG, ΔT is the temperature change, λ_β is the initial central wavelength, and $\Delta\lambda_\beta$ is the central wavelength shift.

The axial stress on the FBG is equal to the tension force F of a spring divided by the cross-sectional area of the fiber. Therefore, a relationship can be established between the hydrophilic rubber probe's axial expansion Δd and the FBG's axial strain $\Delta\varepsilon$.

$$\Delta\varepsilon = \frac{k(x_0 - \Delta d)}{\pi r^2 E} \tag{2}$$

Here, x_0 is the initial spring elongation, k is the spring constant, E is the elastic modulus of the fiber, and r is the radius of the fiber. Neglecting temperature effects, substituting $\Delta\varepsilon$ into Eq. (1) yields the relationship between the central wavelength shift and the axial expansion of the hydrophilic rubber probe:

$$\Delta\lambda_\beta = \frac{k(x_0 - \Delta d)\lambda_\beta(1 - p_e)}{\pi r^2 E}. \tag{3}$$

From the water absorption and desorption characteristics of the hydrophilic rubber probe, it is known that a linear relationship exists between its axial expansion and the soil volumetric water content.

$$\Delta d = \phi\theta_v \tag{4}$$

Here, ϕ is the expansion coefficient of the hydrophilic rubber. Combining Eqs. (3) and (4) yields an expression relating the soil volumetric water content and central wavelength:

$$\theta_v = \frac{\Delta\lambda_\beta \pi r^2 E}{k\lambda_\beta(1 - p_e)\phi} - \frac{x_0}{\phi}. \tag{5}$$

Using Eq. (5), the soil volumetric water content can be determined. However, temperature drift is inevitable in practical measurements. Therefore, temperature compensation was incorporated into the actual design of the sensor.

3. Performance Analysis of Hydrophilic Rubber Probe

To investigate the relationship between water content and axial expansion during water absorption, as well as the moisture sensitivity of hydrophilic rubber probes with different shapes, the rubber was prepared in three configurations, as shown in Fig. 2: (A) a 2 cm cube; (B) a perforated 2 cm cube with a 0.5-cm-diameter central through-hole; (C) a perforated, grid-patterned 2 cm cube with a 0.5-cm-diameter central through-hole and surrounding cuts forming a grid. The cut probes were then encapsulated in 2 × 2 × 4 cm shells featuring permeable holes 0.1 cm in diameter to simulate the sensor's actual working environment. The probes were immersed in water, and the mass of each of the three types was measured at 30 min intervals to determine the corresponding water content. Simultaneously, their axial expansion was measured using a micrometer caliper. The experimental results are presented in Figs. 3 and 4.

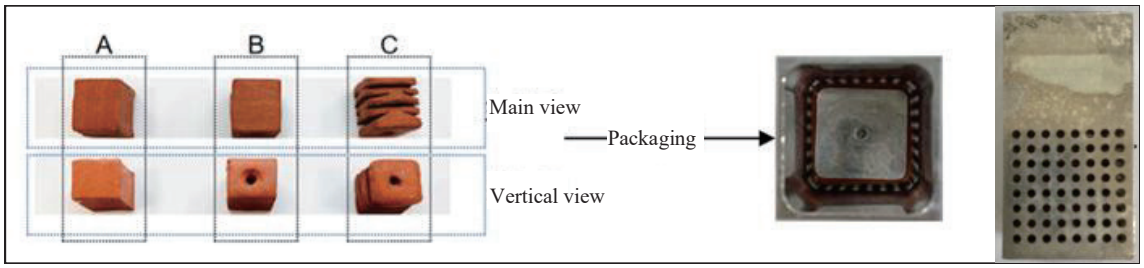

Fig. 2. (Color online) Images of a hydrophilic rubber probe.

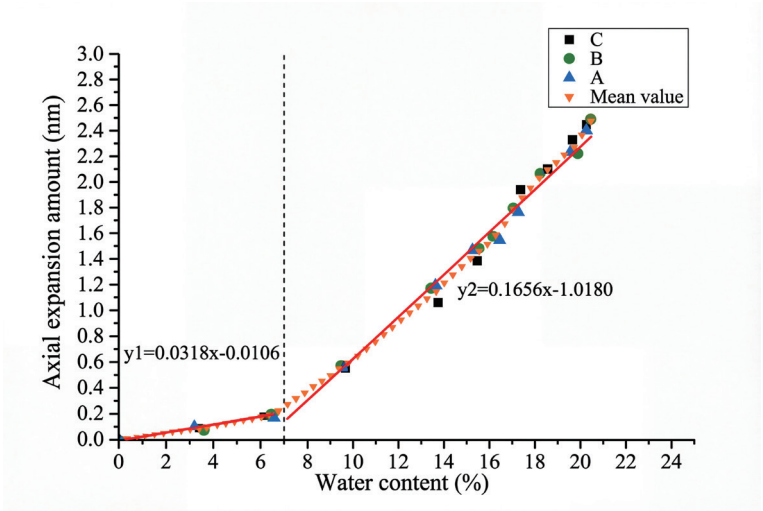

Fig. 3. (Color online) Relationship between axial expansion and water content for the three probe designs.

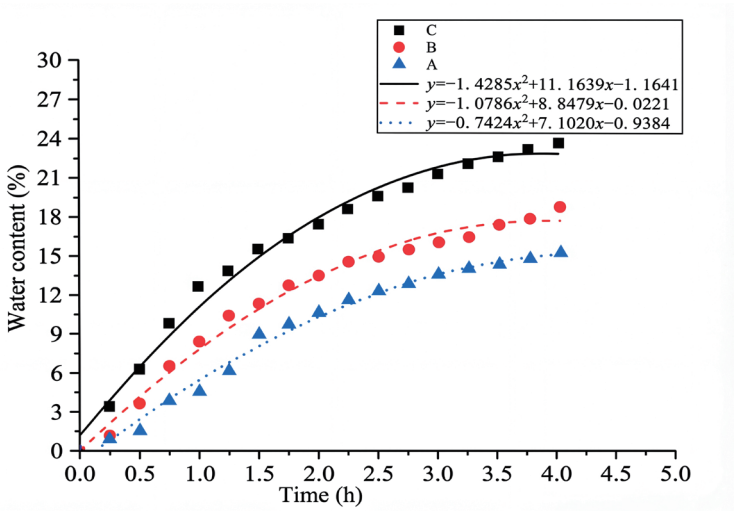

Fig. 4. (Color online) Water absorption rate for the three probe designs.

As shown in Fig. 3, both the moisture content and axial expansion of the three probe types exhibited a monotonically increasing trend during water absorption. With the variation in moisture content, the change in axial expansion for all three probe types was basically the same. After calculating the average values for the three prove types and performing a linear regression, it was found that for moisture contents below 7%, the axial expansion changes by 0.159 mm for every 5% change in moisture content; for moisture contents above 7%, this value increases to approximately 0.9 mm. Figure 4 indicates that the moisture content of all three probe types increases over time. After the same duration, the perforated grid-patterned probe exhibits the largest axial expansion. Therefore, the perforated grid-patterned probe was selected for the sensor design in this study.

4. Performance Analysis of Sensors

4.1 Dynamic response and reproducibility testing

To evaluate the long-term stability of the sensor, its dynamic response and repeatability were tested. The experimental setup consisted of a spectrometer, a broadband light source, an optical circulator, and an acrylic container, with all experiments conducted at a constant temperature of 26 ℃.

The testing process was divided into two stages. The first, the water absorption experiment, involved fixing the sensor inside the acrylic container and injecting a 2 cm layer of water. The central wavelength output by the sensor was measured with the spectrometer at 30 min intervals until the wavelength stabilized, at which point the sensor was removed from the water. The second stage was the water loss (desorption) experiment, where the sensor was placed in a dry environment to dehydrate. Data were again recorded at 30 min intervals until the output stabilized. This entire two-stage process was repeated three times to ensure repeatability.

The experimental results shown in Fig. 5 indicate that the soil moisture sensor requires 5 h to stabilize during the water absorption phase and 8 h during the water loss phase, with a corresponding output wavelength ranging from 1557.7110 to 1557.6420 nm. The calculation of the multiple measurement results yielded a repeatability error of 10% for the sensor.

4.2 Sensitivity and calibration of sensors

Calibration is a critical step in the sensor design and development process. For the calibration experiment, test samples were prepared using typical sandy loam sourced from the Institute of Disaster Prevention Technology. Initially, the collected samples were naturally air-dried, ground, and sieved through a 0.4 mm mesh to remove impurities. Subsequently, the samples were placed in a drying oven at 105 ℃ for 24 h. The required proportions of dry soil and water were calculated to prepare six soil samples with graded volumetric water content levels. Each sample was packed uniformly into a polyvinyl chloride (PVC) testing barrel, and their final volumetric water contents were verified to be 11.2, 15.3, 18.7, 22.5, 26.4, and 31.2% by the oven-drying method.

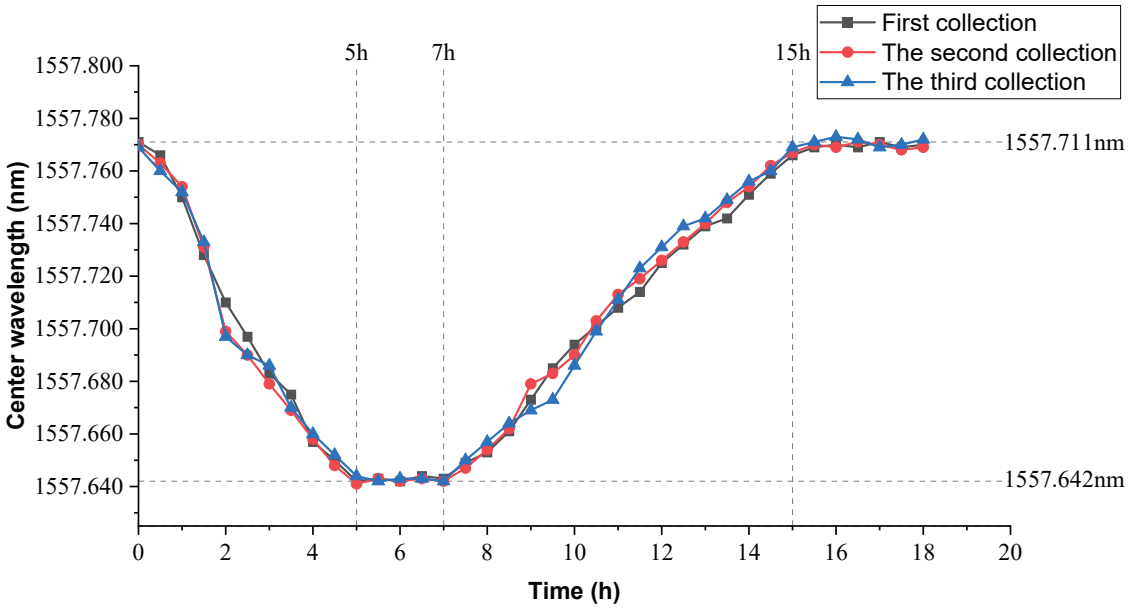

Fig. 5. (Color online) Dynamic response and repeatability test results.

The calibration was performed at an ambient temperature of 26 °C. In the setup depicted in Fig. 6, the sensor was installed in each prepared soil sample and connected to a light source and a spectrometer via an armored optical fiber and an optical circulator. The central wavelength output by the sensor was then recorded by the spectrometer every 0.5 h. The experimental results are presented in Fig. 7.

As seen in Fig. 7, at different soil volumetric water contents, the central wavelength values output by the sensor at a stable state are also different. The higher the volumetric water content, the smaller the central wavelength value and the larger the absolute value of the change in central wavelength. Therefore, by performing a linear regression between the absolute value of the change in central wavelength in a stable state and the soil volumetric water content, the calibration results of the sensor can be obtained. As shown in Fig. 8, the output of the soil moisture sensor has good correlation with the soil volumetric water content, and the coefficient of determination (R^2) reached 0.9659. Additionally, it can be observed that the sensor has high sensitivity as each 10% change in volumetric water content results in an output variation above 0.0047 nm at the central wavelength.

4.3 Experimental analysis of sensor measurement range

Following the method detailed in Sect. 3.2, experimental soil samples were prepared with the five graded volumetric water contents of 11.2, 22.3, 31.5, 40.6, and 49.8%. A sensor was installed in each prepared soil sample, and after its output stabilized, the central wavelength was recorded using a spectrometer. The experimental results are shown in Table 1.

The sensor's permeable holes were protected by an outer polyurethane mesh, which only permits the passage of water molecules. Consequently, when the soil reached saturation and free

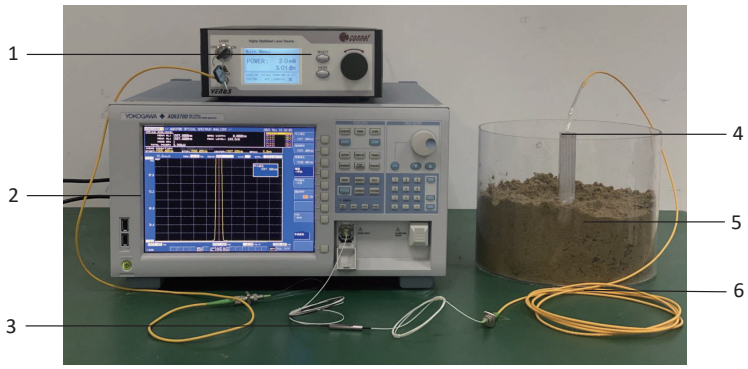

Fig. 6. (Color online) Sensor calibration environment. 1. Broadband light source; 2. Spectrometer; 3. Ring resonator; 4. Moisture sensor; 5. Test soil sample; 6. Armored optical fiber.

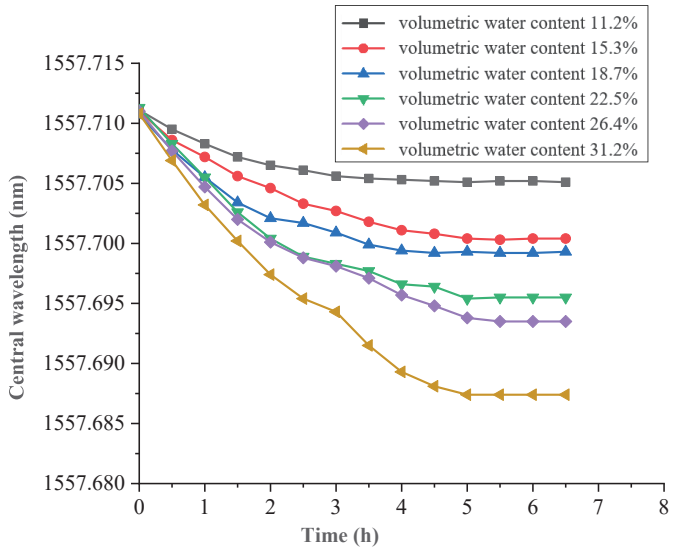

Fig. 7. (Color online) Variations in central wavelength with different soil volumetric moisture contents.

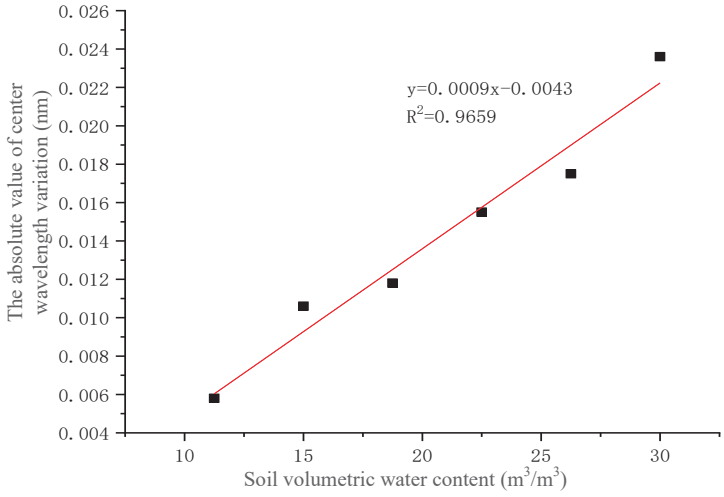

Fig. 8. (Color online) Sensor calibration curve of wavelength shift vs soil water content.

Table 1
Measurement range test results.

Volumetric moisture content (%)	11.1	22.3	31.5	40.6 (Water is separated)	49.8 (Water is separated)
Central wavelength (nm)	1557.7087	1557.6979	1557.6875	1557.6415	1557.6417

water was present, the sensor's output value remained largely unchanged, as shown by the experimental results in Table 1.

4.4 Temperature compensation experiment

In practical applications, FBGs exhibit cross-sensitivity to both strain and temperature, which necessitates temperature compensation. To achieve this, in this study, we employed a dedicated temperature grating for compensation. This grating was an FBG embedded within the sensor that was strain-free and force-free. The temperature-induced error in the strain grating was then corrected by subtracting the wavelength shift of the temperature grating from the total measured wavelength shift.

The performance of the temperature compensation was experimentally verified. The sensor was placed in a thermostatic chamber, and the temperature was increased from 0 to 50 ℃ in 5 ℃ increments, with each step maintained for 20 min. The central wavelength output by the sensor was recorded at each interval using a spectrometer. The results are presented in Fig. 9.

Figure 9 shows that as the temperature increases, the wavelength shifts of both the strain grating and the temperature grating exhibit similar increasing trends. The temperature sensitivity was determined to be 9.76 pm/K for the strain grating and 10.03 pm/K for the temperature grating. Subtracting these two values yields a net temperature sensitivity of 0.35 pm/K for the soil moisture sensor. After temperature compensation, the sensor's temperature sensitivity significantly decreases, thereby minimizing measurement error.

4.5 Experimental analysis of sensor errors

To further validate the sensor's measurement accuracy, six sandy loam samples with similar characteristics other than the unknown volumetric water content were selected. In a comparative experiment, the volumetric water content of each sample was measured using two methods: the standard oven-drying method and the use of the sensor developed in this study. The measurement results are shown in Table 2. Compared with the benchmark oven-drying method, the results show that the sensor has an absolute error ranging from −1.47 to −1.94% and a relative error ranging from −5.3 to 11.6% in measuring the soil volumetric water content. This indicates that the sensor's accuracy meets the requirements for soil moisture measurement.

5. FBG Soil Moisture Measurement System

To enable a long-term, stable, and regional measurement of soil moisture, a comprehensive measurement system was developed on the basis of the sensor designed in this study. As shown in Fig. 10, the system comprises a soil moisture sensor unit and a soil moisture sensor

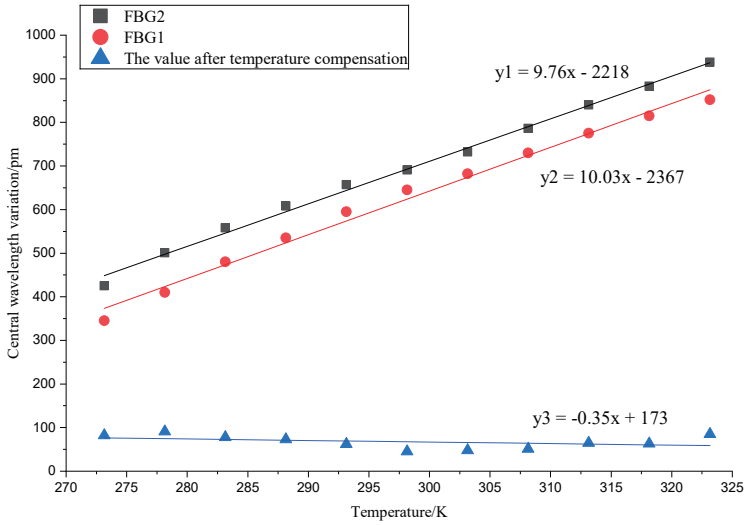

Fig. 9. (Color online) Temperature compensation results for the sensing and compensation FBGs.

Table 2
Comparison of test results.

Sample number	1	2	3	4	5
Oven-drying method (%)	11.32	16.76	23.12	25.53	30.60
Self-made sensors (%)	12.64	15.86	22.17	24.06	32.54
Absolute error (%)	1.32	−0.9	−0.95	−1.47	1.94
Relative error (%)	11.6	−5.3	−4.1	−5.8	6.3

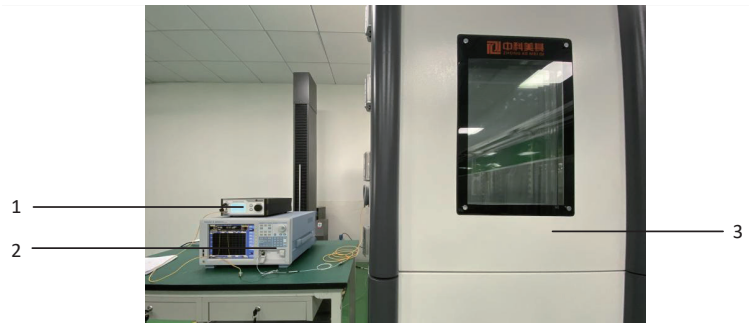

Fig. 10. (Color online) Temperature-compensated experimental environment. 1. Broadband light source; 2. Spectrometer; 3. Temperature chamber.

demodulation unit. The sensor unit consists of multiple FBG-based soil moisture sensors connected in series, which enables distributed measurements. The soil moisture sensor unit transmits the detected volumetric water content information to the soil moisture sensor demodulation unit as optical signals via multiple FC-connected fiber channels.

The soil moisture sensor demodulation unit is composed of six main modules: a MEMS light switch, a C band broadband light source module, a ring device, a Bay Spec low-speed optical

wavelength demodulation module, a power supply unit, and a digital I/O card. The power supply unit provides power to the C band broadband light source module and the Bay Spec low-speed optical wavelength demodulation module.

The system operates as follows: a broadband optical signal from the C band broadband light source module is routed through the MEMS light switch to select a specific sensor. The signal is then directed by the ring device and injected into the sensor's FBGs via an FC jumper. Changes in soil moisture and temperature cause a shift in FBG's Bragg wavelength, causing it to reflect a narrow band of light corresponding to its current state. This reflected signal travels back through the ring device and enters the Bay Spec low-speed optical wavelength demodulation module for filtering. The demodulation module converts the optical wavelength data into a digital electrical signal, and the digital I/O card facilitates communication between the module and a host computer.

As shown in Fig. 11, the power supply unit exclusively powers the soil moisture sensor demodulation unit. The soil moisture sensor unit itself is passive, requiring no electrical power, and is simply installed directly into the soil. This passive sensor unit operates by converting changes in soil volumetric water content into strain on the FBG. This strain alters the Bragg wavelength of the reflected light, which is how data is encoded. Therefore, to acquire data, the demodulation unit simply sends an optical signal to the sensor and demodulates the reflected optical signal.

FBG sensing signals are inherently suitable for long-distance transmission because of their strong immunity to electromagnetic interference, low signal loss, and high transmission speed. Consequently, the soil moisture sensor unit and the demodulation unit can be installed in separate locations. As shown in Fig. 12, they are connected by an armored optical fiber for robust data communication. This passive sensing approach resolves the common challenge of supplying power to sensors in the field. The overall system features low power consumption and high environmental adaptability, making it ideal for the long-term, stable, regional monitoring of soil moisture, particularly in challenging field environments with limited power access.

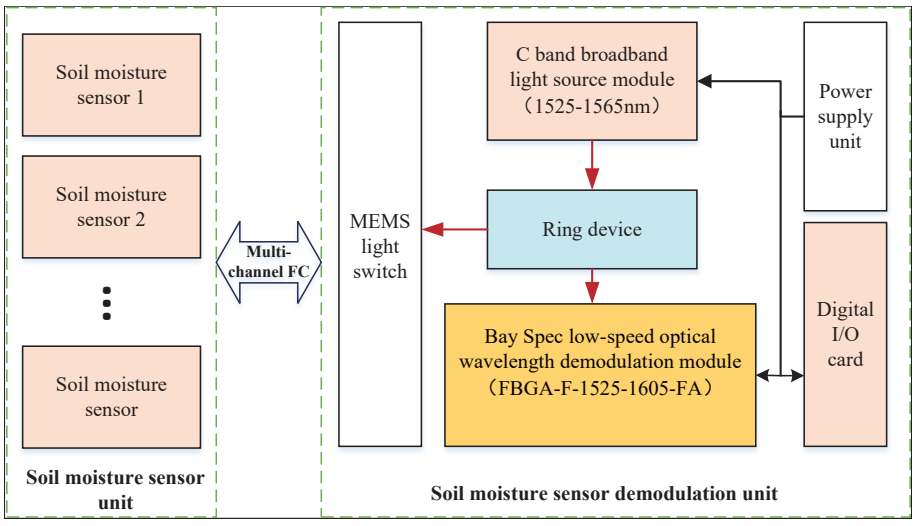

Fig. 11. (Color online) Block diagram of a soil moisture measurement system.

6. Field Dynamic Testing

A flower bed at the College of Disaster Prevention Science and Technology was selected as the site of a field dynamic test, using soil identical to the samples from the calibration experiments. The site is located in the Yanjiao Economic Development Zone, Langfang, Hebei Province. The experimental setup is shown in Fig. 13. For the test, a soil moisture sensor was installed at a depth of 25 cm and monitored for 100 h.

The data presented in Fig. 14 show the dynamic changes in soil volumetric water content over the testing period. From 0 to 17.5 h, the soil volumetric water content slowly decreased as the temperature rose. Subsequently, between 17.5 and 27.5 h, intermittent watering at the test site led to a significant increase in volumetric water content. From 27.5 to 60 h, the volumetric water content declined again, primarily owing to water permeation. Increased evaporation caused by

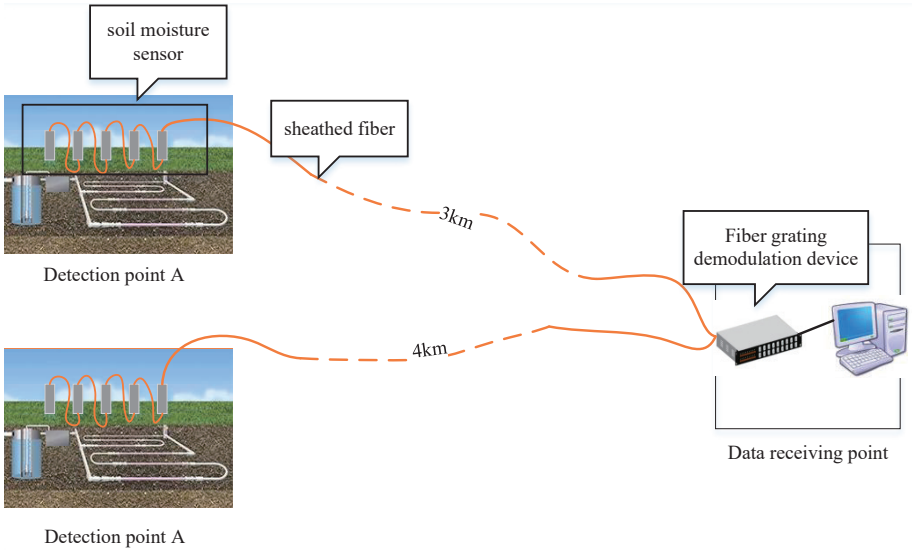

Fig. 12. (Color online) Schematic diagram of the practical application of the soil moisture measurement system.

Fig. 13. (Color online) Practical application of the soil moisture measurement system. 1. Soil moisture sensor demodulation unit; 2. Soil moisture sensor unit; 3. Personal computer (PC); 4. Power supply.

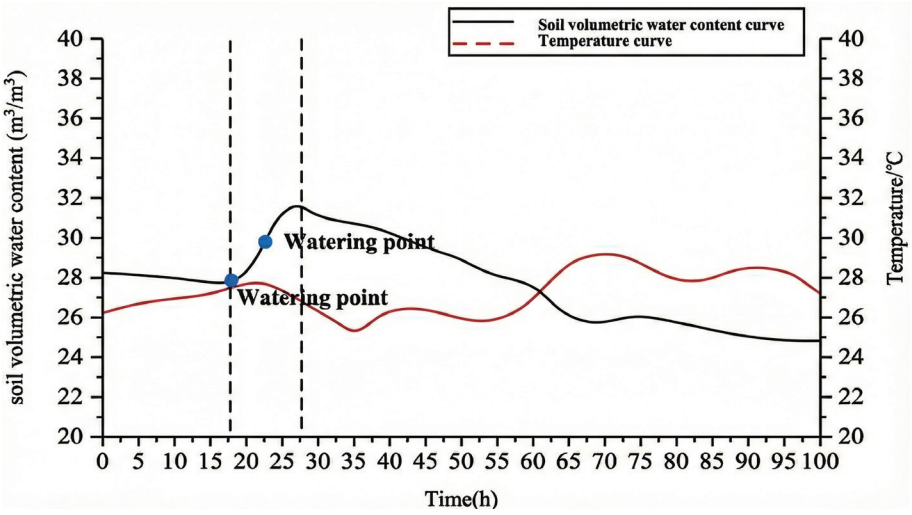

Fig. 14. (Color online) Field test results from 100-hour soil moisture and temperature monitoring.

temperature variations during this period also contributed to a slow decline, resulting in overall moisture levels lower than those in the initial 0–17.5 h phase.

The experimental results demonstrate that the sensor's output consistently tracks the changes in soil volumetric water content over the long term, without abrupt fluctuations or instability. This performance confirms the sensor's suitability for the long-term, stable monitoring of soil moisture.

6. Conclusions

In this study, we constructed and tested a soil moisture sensor based on FBG technology. The sensor features an expansive structural design, enabling long-term, stable, and regional soil moisture measurements. The water absorption and expansion characteristics of hydrophilic rubber probes with different shapes were analyzed. The perforated grid-patterned probe was found to exhibit superior performance and was therefore selected for the final sensor design. The sensor's performance was thoroughly evaluated. Performance tests demonstrated stabilization times of 5 h for water absorption and 8 h for water desorption. The sensor exhibited a high sensitivity, with a 10% change in volumetric water content inducing a wavelength shift above 0.0047 nm. The upper detection limit was determined to be the soil's saturated water content. After temperature compensation, the residual temperature sensitivity was effectively reduced to 0.35 pm/K. Accuracy validation against the oven-drying method revealed an absolute error between −1.47 and −1.94% and a relative error between −5.3 and 11.6%. Finally, a complete measurement system was constructed and successfully demonstrated in field experiments, confirming the sensor's practical applicability and reliable performance in real-world monitoring.

Acknowledgments

This work was supported by the Science and Technology Innovation Program for Postgraduate students in IDP subsidized by Fundamental Research Funds for the Central Universities (Grant No. ZY20250323).

References

1 H.-H. Zhu, Y.-X. Huang, H. H. A. Garg, G.-X. Mei, and H.-H. Song: Int. J. Geosynth. Ground Eng. **8** (2022) 8. https://doi.org/10.1007/s40891-022-00360-8
2 A. M. Diniz, M. A. V. Boas, M. B. Remor, J. A. C. Siqueira, and L. K. Tokura: J. Agric. Sci. **11** (2019) 192. https://doi.org/10.5539/jas.v11n2p192
3 H. Li, W. Yu, and Z. Wang: Trans. CSAM **51** (2020) 213. https://doi.org/10.6041/j.issn.1000-1298.2020.02.023
4 Z. Gao, W. Liu, and Y. Zhao: Trans. CSAM **47** (2016) 185. https://doi.org/10.6041/j.issn.1000-1298.2016.11.025
5 Q. Sheng, M. Ni, X. Zhang, and P. Li: Trans. CSAM **51** (2020) 324. https://doi.org/10.6041/j.issn.1000-1298.2020.05.035
6 X. Wu, X. Y. Li, P. W. Li, T. W. Lei, W. Wang, J. Liu, and Y. Z. Feng: Trans. CSAE **25** (2009) 33. https://doi.org/10.3969/j.issn.1002-6819.2009.03.006
7 J. N. Li, T. S. Hong, R. J. Feng, Y. J. Xue, and Q. F. Dai: Trans. CSAE **27** (2011) 216. https://doi.org/10.3969/j.issn.1002-6819.2011.08.037
8 J. Luo, Q. Liu, Z. Zhou, and Q. Wei: Measurement **159** (2020) 107618. https://doi.org/10.1016/j.measurement.2020.107618
9 K. Zhang, X. X. Liu, J. Tian, C. Ma, and Y. D. Cao: Ship Stand. Eng. **55** (2022) 20. https://doi.org/10.14141/j.31-1981.2022.01.003
10 X. F. Huang, D. R. Sheng, K. F. Cen, and H. Zhou: Sens. Actuators, B **127** (2007) 518. https://doi.org/10.1016/j.snb.2007.05.007
11 K. Čápová, L. Velebil, and J. Včelák: Sensors **20** (2020) 1661. https://doi.org/10.3390/s20061661
12 G. Breglio, R. Bernini, G. M. Berruti, F. A. Bruno, S. Buontempo, S. Campopiano, E. Catalano, M. Consales, A. Coscetta, A. Cutolo, M. A. Cutolo, P. D. Palma, F. Esposito, F. Fienga, M. Giordano, A. Iele, A. Iadicicco, A. Irace, M. Janneh, A. Laudati, M. Leone, L. Maresca, V. R. Marrazzo, A. Minardo, M. Pisco, G. Quero, M. Riccio, A. Srivastava, P. Vaiano, L. Zeni, and A. Cusano: Sensors **23** (2023) 3187. https://doi.org/10.3390/s23063187
13 D. Cao, H. Fang, F. Wang, H. Zhu, and M. Sun: Sensors **18** (2018) 4431. https://doi.org/10.3390/s18124431
14 J. S. Hallett, M. Partridge, S. W. James, D. Tiwari, T. Farewell, S. H. Hallett, and R.P. Tatam: Proc. SPIE 10323, 25th Int. Conf. Optical Fiber Sensors (2017) 103232J. https://doi.org/10.1117/12.2263427
15 D.-F. Cao, H.-H Zhu, B. Wu, J.-C. Wang, and S. K. Shukla: Eng. Geol. **290** (2021) 106197. https://doi.org/10.1016/j.enggeo.2021.106197
16 H. Wang, S. Gao, X. Yue, X. Cheng, Q. Liu, R. Min, H. Qu, and X. Hu: Sensors **21** (2021) 6946. https://doi.org/10.3390/s21216946
17 M. Leone, S. Principe, M. Consales, R. Parente, A. Laudati, S. Caliro, A. Cutolo, and A. Cusano: Sensors **17** (2017) 1451. https://doi.org/10.3390/s17061451
18 J.-Y. Guo, B. Shi, M.-Y. Sun, W. Cheng, C.-C. Zhang, G.-Q. Wei, and X. Wang: Measurement **188** (2022) 110415. https://doi.org/10.1016/j.measurement.2021.110415
19 M. Leone: A Rev. Results Opt. **7** (2022) 100213. https://doi.org/10.1016/j.rio.2022.100213
20 M. I. Abdulraheem, Y. Xiong, W. Zhang, H. Chen, H. Zhang, and J. Hu: Int. J. Precis. Eng. Manuf. **25** (2024) 1499. https://doi.org/10.1007/s12541-024-01015-6
21 Q. Liu and X. He: Mater. Rep. **32** (2018) 242. https://doi.org/10.11896/j.issn.1005-023X.2018.S1.054
22 C. E. Campanella, A. Cuccovillo, C. Campanella, A. Yurt, and V. M. N. Passaro: Rev. Technol. Appl. Sens. **18** (2018) 3115. https://doi.org/10.3390/s18093115